PAPER

Check for updates

Pseudo 2-dimensional nanostructures of metal oxides for high-performance supercapacitors†

Debabrata Mandal, [a] Sudipta Biswas, [b] Ananya Chowdhury[b] and Amreesh Chandra *[ab]

Recently, high performance supercapacitors based on hollow nanostructures have been reported. The enhanced behaviours are directly attributed to the higher specific surface area of hollow particles. It is shown here that this is an oversimplified explanation. If only the surface area was driving the enhancement then other solid morphologies, with a higher specific area, should show better performance. Careful modelling and simulation studies show that hollow structures can actually be viewed as pseudo 2-dimensional (2-D) materials. This leads to performance similar to that reported in 2-dimensional materials ranging from metal oxides to MXenes. Therefore, the underlying reasons, inducing the performance enhancement, are explained for the first time. The theoretically predicted behaviour is proven experimentally by using CeO_2 hollow and solid nanostructures as the test samples. The result also establishes the importance of using hollow structures of rare-earth oxides, if they are to be used in supercapacitors. Finally, it is shown that the future direction should involve the combination of a pseudo 2-D structure with a real 2-D-carbon based electrode. The use of 2-D gC_3N_4, with a lower specific surface area than activated carbon but much higher specific capacitance, reaffirms the inferences that the role of the specific surface area is mostly over-estimated in supercapacitors.

1. Introduction

Self-assembled hierarchical nanostructures are slowly superseding most of the conventional nanostructures for use in supercapacitor electrodes. These morphologies intrinsically show high surface area, tunable porosity and packing density, which can be easily modulated. The last decade has seen tremendous interest in 2-dimensional (2-D) nanostructures.[1–3] These can have fascinating semiconducting properties owing to modulated confinement, optical properties because of significant change in the band structures, electrical or electrochemical properties associated with their surface states and enhanced accessible active sites.[2,4–6] The interest in 2-D nanostructures was initiated by the fascinating world of graphene. Novel alternatives to graphene such as MXenes are taking the interest in 2-D nanostructures to the next level.[4,7] In terms of applicability, these materials would be useful in energy storage and harvesting devices, 5G antennas, electronics, smart textiles, EMI shielding, biomaterials, sensors, optoelectronics, environmental applications, *etc.*[3,8–12]

The major limitations associated with most 2-D materials are low yield synthesis protocols, reproducibility, stability, and limited operating temperature range.[13,14] Hence, conventional or almost hierarchical nanostructures of metal oxides are still more preferred. For example, in energy storage devices, nano metal oxides do deliver slightly lower specific capacitance, but compensate by ensuring higher stability, cost-effectiveness and long life.[15] Ideally, if 2-D structures of metal oxides can be easily produced then they would be most preferred. There have been few reports suggesting that ultrasonication-driven exfoliation of oxides like MnO_2, Mn_3O_4, NiO, and Co_3O_4 can be obtained.[16–23] But, the structural stability and phase integrity of such materials still remains questionable.

In this paper, it is shown that the fast emerging hollow nanoparticles can be viewed as pseudo-2-D nanostructures. The term pseudo is used because the materials are 3-dimensional in reality but the structures stabilize in a way that it actually simulates a layered material-like response. Using molecular dynamics and simulation, it is shown that these structures pack themselves in an arrangement that also leads to a stable channel for ion intercalation. Thus, these materials become extremely useful to energy storage devices. There have been studies in the recent past, where hollow metal oxides have been used to obtain high-performance supercapacitors and batteries. All those papers attributed the observed high performance to the higher surface area of hollow structures. Never has there

[a] *School of Nano Science and Technology, Indian Institute of Technology Kharagpur, India. E-mail: achandra@phy.iitkgp.ac.in*

[b] *Department of Physics, Indian Institute of Technology Kharagpur, Kharagpur, 721302, India*

† Electronic supplementary information (ESI) available. See DOI: https://doi.org/10.1039/d2ma00366j

been an attempt to carefully understand the origin of the higher performance in these structures. If one sees the real 2-D carbon materials, which have lower specific surface area than activated carbon, it is clear that they are able to deliver higher specific capacitance. Therefore, the role of the specific surface area of electrode materials used in supercapacitors is over estimated. It is the accessible area that plays the important role. The novel architecture of a 3-D-hollow structure is able to simultaneously fulfill both these requirements *i.e.* high surface area and layered like morphology. This paper opens a new dimension in the research of 2-D nanostructures.

It is now becoming clear that asymmetric or hybrid type supercapacitors would be more preferred in future applications.[24–26] Therefore, combining a 2-D metal oxide-based pseudocapacitive electrode with a 2-D carbon-based EDLC-type electrode would be the way forward.[27] In this paper, using pseudo-2-D CeO_2 and real 2-D gC_3N_4 electrodes, the usefulness of this strategy is unequivocally established. The use of CeO_2 in supercapacitors has been reported earlier but none of the studies have used hollow structures and hence the specific capacitance value has remained low.[27,28] To increase the value, composites of CeO_2 with graphene, *etc.* have been investigated by earlier workers.[29,30] But this just leads to cost escalation, without appreciable enhancement. Our studies further show that pseudo-2-D structures of rare earth oxides can also become useful and deliver high specific capacitances. The results are proven by comparing the results delivered by conventional solid nanoparticles of CeO_2. The asymmetric supercapacitors can operate up to 1.3 V, achieving a maximum specific capacitance of 60 F g^{-1} at a current density of 1 A g^{-1}. Moreover, the fabricated hollow $CeO_2 \| gC_3N_4$ device exhibits an excellent energy density of ~ 14.33 W h kg^{-1} with a power density of ~ 703 W kg^{-1}, making it suitable for various applications.

2. Materials and method

2.1 Material synthesis

The solid and hollow nanostructures of CeO_2 and 2-D graphite carbon nitrate were used as the positive and negative electrode materials for the study. The synthesis protocol of all the materials is given in the ESI.†

2.2 Material characterization

The morphology of the materials was analysed by scanning electron microscopy (SEM, CARL ZEISS SUPRA 40) and transmission electron microscopy (TEM, FEI-TECNAI G220S-Twin operated at 200 kV). Brunauer–Emmett–Teller (BET) surface area and porosity were measured with a Quantachrome Novatouch analyser. The phase formation of the materials was confirmed by XRD analysis, using a Rigaku Miniflex diffractometer, with Cu Kα ($\lambda = 0.15406$ nm) as the incident radiation. A Horiba Scientific SZ-100 nanoparticle analyser was used for the particle size and zeta potential measurements.

2.3 Electrochemical measurement

The electrodes were prepared by mixing 80 wt% CeO_2, 10 wt% activated carbon and 10 wt% polyvinylidene fluoride in acetone. The mixture was stirred continuously at 80 °C for 8 h, to obtain a homogeneous slurry. The slurry was coated onto a graphite sheet (1 cm × 1 cm) and dried in a vacuum oven for ~ 12 h. Cyclic voltammetry (CV), galvanostatic charge–discharge (CD) and impedance spectroscopy (EIS) were performed in 3 M KOH, using a Metrohm Autolab (PGSTAT302N) potentiostat, in both three-electrode and device configurations. For the three-electrode measurements, platinum wire and Ag/AgCl/3.0 M KCl were used as counter and reference electrodes, respectively. The electrochemical analysis of the asymmetric supercapacitor device was performed using CR2032 type cells. Whatman glass fibre was used as a separator in the asymmetric device.

2.4 Simulation of the pseudo-2-D structures

Molecular dynamic simulations were performed using the LAMMPS software package. The simulation, to visualize the structures, was performed initially by considering one sphere only. The model was extended to construct the adjacent spheres and the closest approach was reduced to make the spheres just touch side-by-side. The crystal structure for the material and bond energy was fixed according to the data obtained from the XRD. A cubic simulation box (600 nm × 600 nm × 600 nm), with periodic boundaries, was considered. The system energy was minimized during the simulation. The simulation was performed at a time step of 1 millisecond.

3. Results and discussion

3.1 Structural and morphological characterization

The structure, phase and purity of the CeO_2 hollow and solid structures were determined by the X-ray diffraction analysis. The X-ray diffraction pattern of both hollow and solid CeO_2 is shown in Fig. 1(a). The formation of the crystalline and cubic phase, confirmed using JCPDS card no. (81-0792), in both types of CeO_2 nanostructures, was discernible.[31] No impurity peak was detected in the XRD patterns. The average crystallite size was ~ 5.70 nm for hollow CeO_2 and ~ 5.29 nm for the solid particles. The unit cell dimensions and microstrain estimated in both the CeO_2 nanostructures are given in Fig. S1 and Table S1 (ESI†), respectively. The particle size distribution of the material is shown in Fig. S2 (ESI†). The mean particle size of the hollow and solid CeO_2 was estimated as ~ 315 and 260 nm, respectively. This indicated that both the structures possess high homogeneity and narrow distribution. Fig. 1(b) depicts the Raman spectra, showing the presence of a phonon mode at 460 cm^{-1}, which is linked to the F_{2g} mode. This mode confirmed the cubic fluorite structure of hollow CeO_2.[32] It appears due to the symmetric Ce–O stretching vibration, which is very sensitive towards defects/disorder in the structure. The peaks at 260 cm^{-1} and 600 cm^{-1} could be attributed to the second-order transverse acoustic (2TA) mode and defect induced (D) modes.[33]

The XPS profiles of both the hollow and solid CeO_2 are given in Fig. S3(a and b) (ESI†), respectively. Fig. S3(c and d) (ESI†)
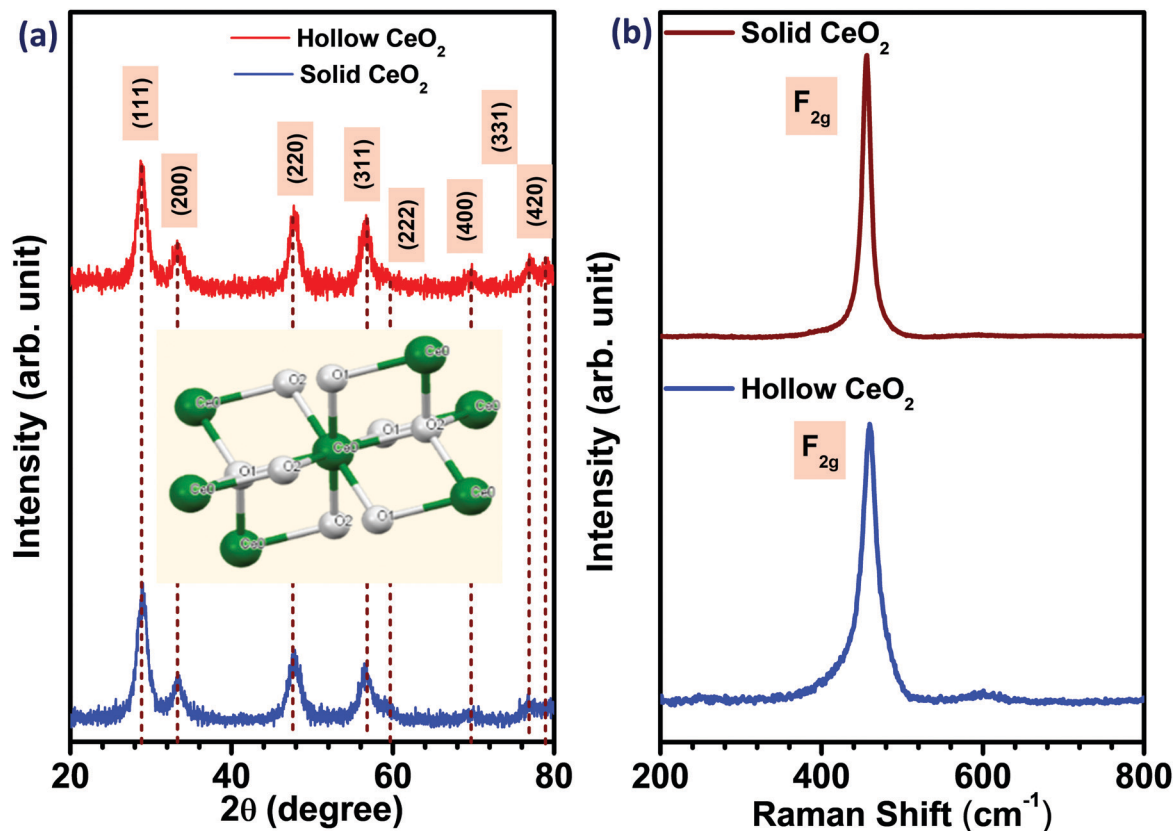
Fig. 1 (a) XRD, and (b) Raman spectra of hollow and solid CeO$_2$.

show the FTIR spectroscopy results of both the CeO$_2$ nano-structures. The absorption bands at 3663 cm^{-1} and 1554–1624 cm^{-1} could be attributed to the stretching and bending mode, respectively. The CO$_2$ absorption on the surface of the material was observed at 2364 cm^{-1}. The stretching bond of O–C–O was found at 1376 cm^{-1}. The formation of the CeO$_2$ was confirmed by the bending mode of Ce–O–Ce, appearing below the 650 cm^{-1} regions.[34] The peak at around 431 cm^{-1} was attributed to the vibration related stretching mode of O–Ce–O.[14] Fig. S4(a and c) (ESI†) depict the nitrogen adsorption–desorption type IV isotherm of the hollow and solid CeO$_2$ nanostructures, showing the capillary condensation at high relative pressure. The BET specific surface area of the hollow CeO$_2$ nanostructure was ∼154 m^2 g^{-1} and that for the solid structure was ∼107 m^2 g^{-1}. The pore size distribution indicated microporous nature, with an average pore diameter of ∼1.51 and 1.68 nm, for the solid and hollow structures, respectively, as shown in Fig. S4(b and d) (ESI†). The zeta potential revealing the average surface charge of solid and hollow CeO$_2$ is shown in Fig. S5(ESI†).

The enhancement in the electrochemical properties of the transition metal oxides is directly related to their particle morphology.[35] To obtain the morphology related information of the synthesized materials, SEM and TEM measurements were performed and the corresponding micrographs are shown in Fig. 2(a)–(d). The results suggested the formation of hollow nanospheres, as well as solid nanoparticles. Along with the morphology of the material, the following information could be

obtained from the SEM and TEM results: (a) size of the hollow nanospheres, (b) inner dimension of the cavity, (c) width of the nanospheres, and (d) homogeneity. The SEM result clearly
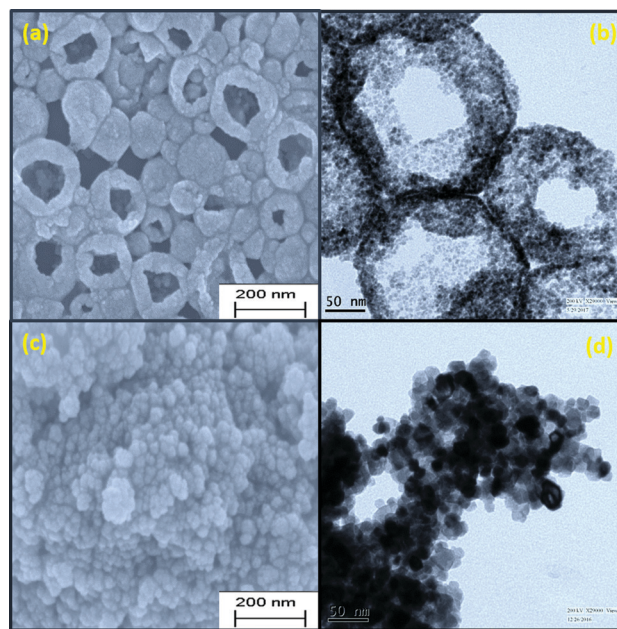

Fig. 2 (a and c) SEM and (b and d) TEM micrographs of hollow and solid CeO$_2$, respectively.
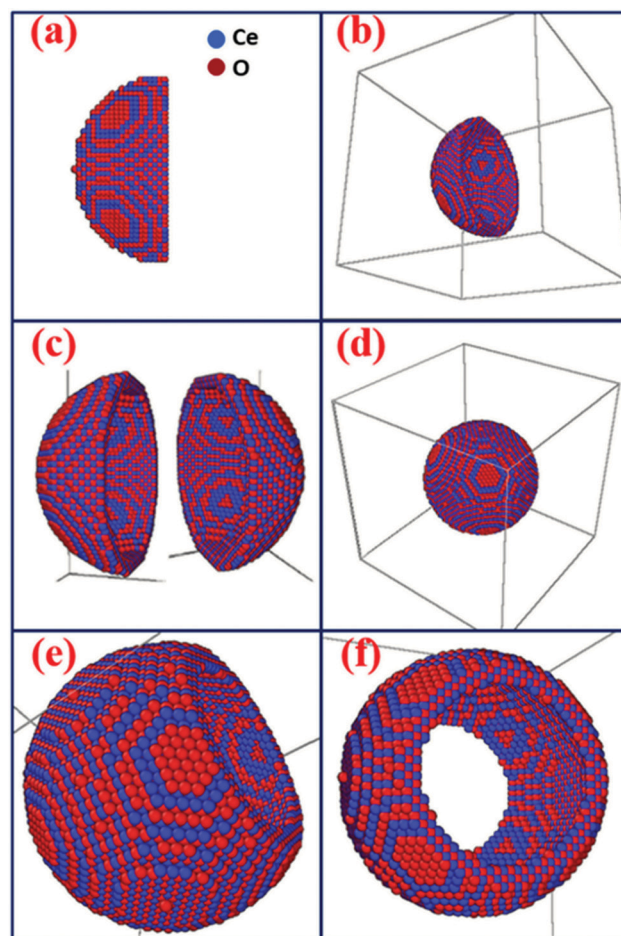
suggested that smaller grains were wrapped along the boundary, leading to the hollow nanospheres. The size of the hollow nanospheres was in the range of 120–200 nm. The diameter of the cavity was ∼60–80 nm. The wall thickness of the nanospheres was ∼30 nm. The size of the solid CeO$_2$ nanoparticles was found to be in the range of 15–25 nm, as calculated from SEM pictures. The presence of Ce and O atoms in both hollow and solid nanostructures is confirmed by elemental mapping analysis, as shown in Fig. S6 and S7 (ESI†), respectively. The TEM micrograph confirmed that a low precursor concentration helps in the growth of hollow morphologies. The cavity was suppressed with increasing concentration of precursor, leading to porous morphologies at higher concentrations.[36] TEM micrographs also indicated the uniform distribution of spherical grains in the boundary of the hollow structures. These small grains were around ∼5–10 nm in size. For solid nanoparticles, the size of each of the small particles was around 5–12 nm. The selected area energy diffraction (SAED) patterns of both types of CeO$_2$ structures confirmed the polycrystalline nature, as shown in Fig. S8 (ESI†). All the rings of the SAED patterns corroborated the XRD data. The EDX result, confirming the presence of elements Ce and O, is given in Fig. S9 (ESI†).

3.2 Hollow particles as a pseudo 2-D nanostructure

Until now, most studies have suggested the hollow or cage frame type structures as better performing materials because they have higher surface area. As discussed earlier, it is now becoming clear that the role of the surface area of metal oxide particles used in supercapacitors is slightly overestimated. It has been reported that a surface area increase of 75 to 100% in solid to hollow structures can lead to 75 to 100% increase in the specific capacitance.[37] But a similar increase in surface area of a given metal oxide, with a different solid morphology, does not lead to such enhancement in specific capacitance.[38] Therefore, there must be additional underlying reasons that drive this increased electrochemical performance. The result discussed below shows that the hollow structure can behave like a pseudo-2-D structure, which leads to their higher performance. The formation of the hollow structures, as an extended form of layered structure, can be explained by using molecular dynamics. The details of coding and energy minimization procedure used during the assembling of hollow particles are described in the ESI.† Scheme 1(a)–(d) show the simulated structures of the hollow CeO$_2$. Scheme 1(e) shows the hollow structure with one side opening and Scheme 1(f) shows the hollow structures with two side openings, simulated by LAMMPS. During the simulation, the lattice parameters obtained from XRD analysis were utilized to construct the building blocks. Here the lattice parameters for the nanosphere were $a = b = c = 5.425$ Å.

It can be seen that a part of the surface on the hollow structure can be taken as the 2-D structure, as depicted in Scheme 2(a). By considering the thickness of the sphere to be small, these structures can be considered as a pseudo-2-D structure. With the curvature of the spherical surface tending towards zero, these structures can also be taken as a planar 2-D structure. From the outside, it looks like a solid sphere but, from inside, it will be a curved 2-D structure, and hence it can be

Scheme 1 (a) Half sphere is constructed, (b) 3-D view of Scheme 1(a), (c) two halves of the sphere, (d) a whole spherical structure of CeO$_2$, (e) sphere with one side opening, and (f) CeO$_2$ sphere with two side opening.

called a pseudo-2-D structure. The term pseudo is used because the structure is closed from the outer side and is not a real 2-D structure. Mathematically, it is already known that hollow surfaces, with thin boundaries, simulate a 2-D layered structure.

Duan *et al.* proposed that the triangular channel among three hollow spheres is important for transportation and diffusion.[39] On simulating hollow spherical particles and bringing them together to obtain a dense material, an interesting feature manifested itself. This was the stabilization of the channels between the particles. Scheme 2(c) shows the three-particle attachment forming a channel for ion diffusion. Such stable channels are quite useful for electrolyte or fluid flow.

The cross-sectional area of these channels was calculated, by considering homogeneous particle size and distribution:
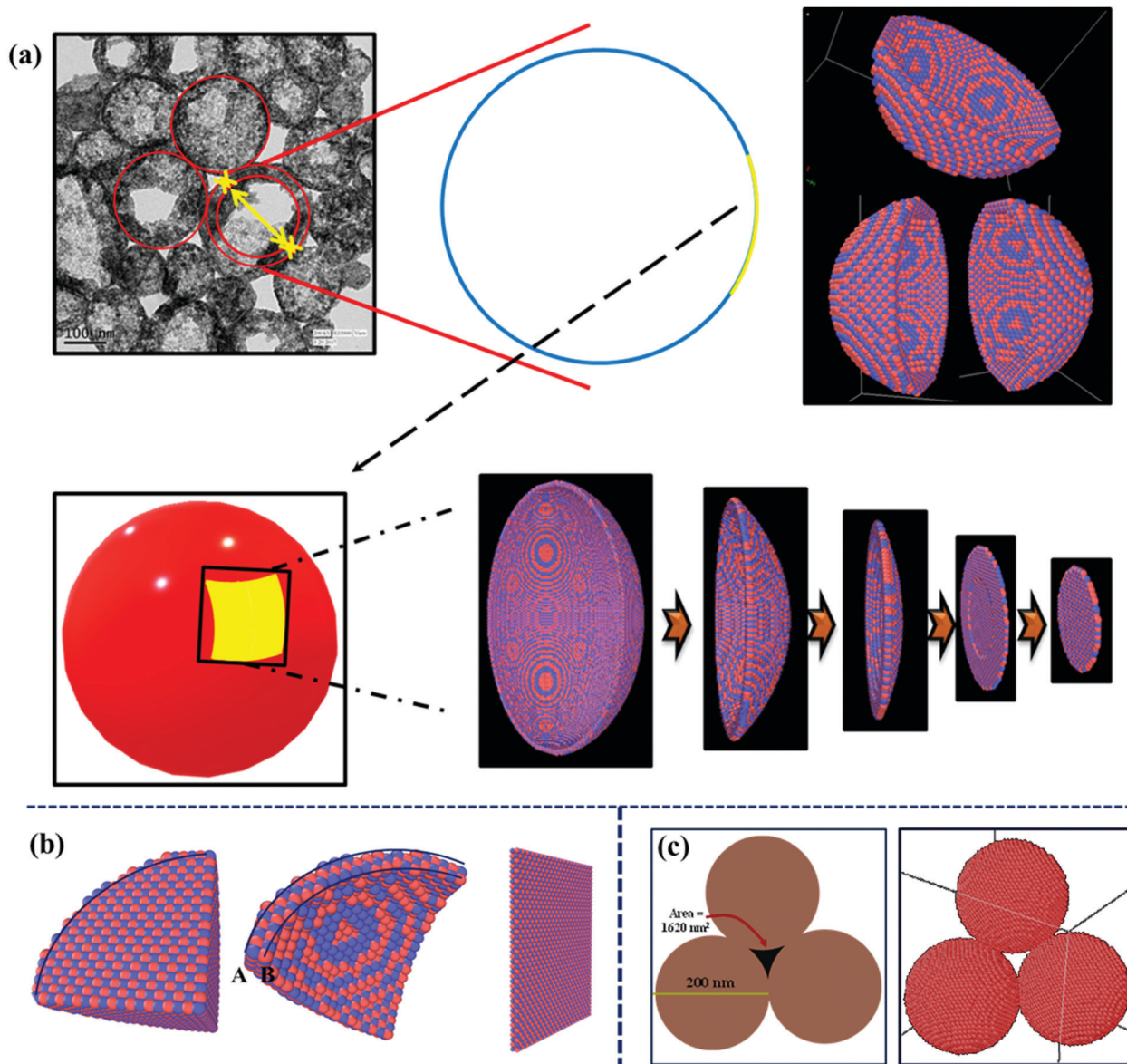
Area of the channel = blank triangular area – area of the spherical sections.

Part of the sphere = 3 × Area of each part circle = half of a sphere.

Here, we have considered that all the particles have the same size, *i.e.*

$$S = \frac{\sqrt{3}d^2}{4} - \frac{\pi d^2}{8}$$

Scheme 2 (a) Visualizing the hollow structure with LAMMPS, (b) the molecular contribution towards electrochemical performance in solid, hollow and planar CeO$_2$, and (c) interparticle channel formed by three hollow structures.

where S is the area of the channel (shaded in black), and d is the outer diameter of the hollow sphere (taking the radius as 200 nm from the TEM image). The calculated channel area = 1620 nm^2. This would facilitate faster and higher ion diffusion. This can be proven by further calculations and estimating the diffusion coefficient in the hollow structure and comparing the value with that obtained using solid structures.

3.2 (a) Diffusion parameter calculation

According to the Randles–Sevcik equation, the CV peak current (I_p) is directly proportional to the analyte concentration C, as described by the following simplified equation:[40]

$$I_p = 0.4463nFAC\left(\frac{nFD\nu}{RT}\right)^{\frac{1}{2}}$$

where n, F, A, D, ν, R, and T denote the number of electrons involved in the reaction of the redox couple, Faraday's constant (96 485 C mol^{-1}), the active surface area of the electrode, diffusion coefficient, scan rate, the universal gas constant (8.314 J mol^{-1} K) and the absolute temperature (K), respectively. From the slope of the I_p vs. $\nu^{1/2}$ graphs shown in Fig. S10(a and b) (ESI†), the diffusion coefficients of the hollow and solid CeO$_2$ electrodes were calculated in 3 M KOH electrolyte. The estimated diffusion coefficients were 1.17×10^{-11} and 0.24×10^{-11} cm^2 s^{-1} for hollow and solid CeO$_2$ nanostructures, respectively. It is clear that the hollow particle-based material had $\sim$5 fold increment in the diffusion coefficient value as shown in Fig. S11(a and b) (ESI†). Higher diffusion also ensures higher charge storage. These results were corroborated by the zeta potential data shown in Fig. S5 (ESI†). The zeta potential values
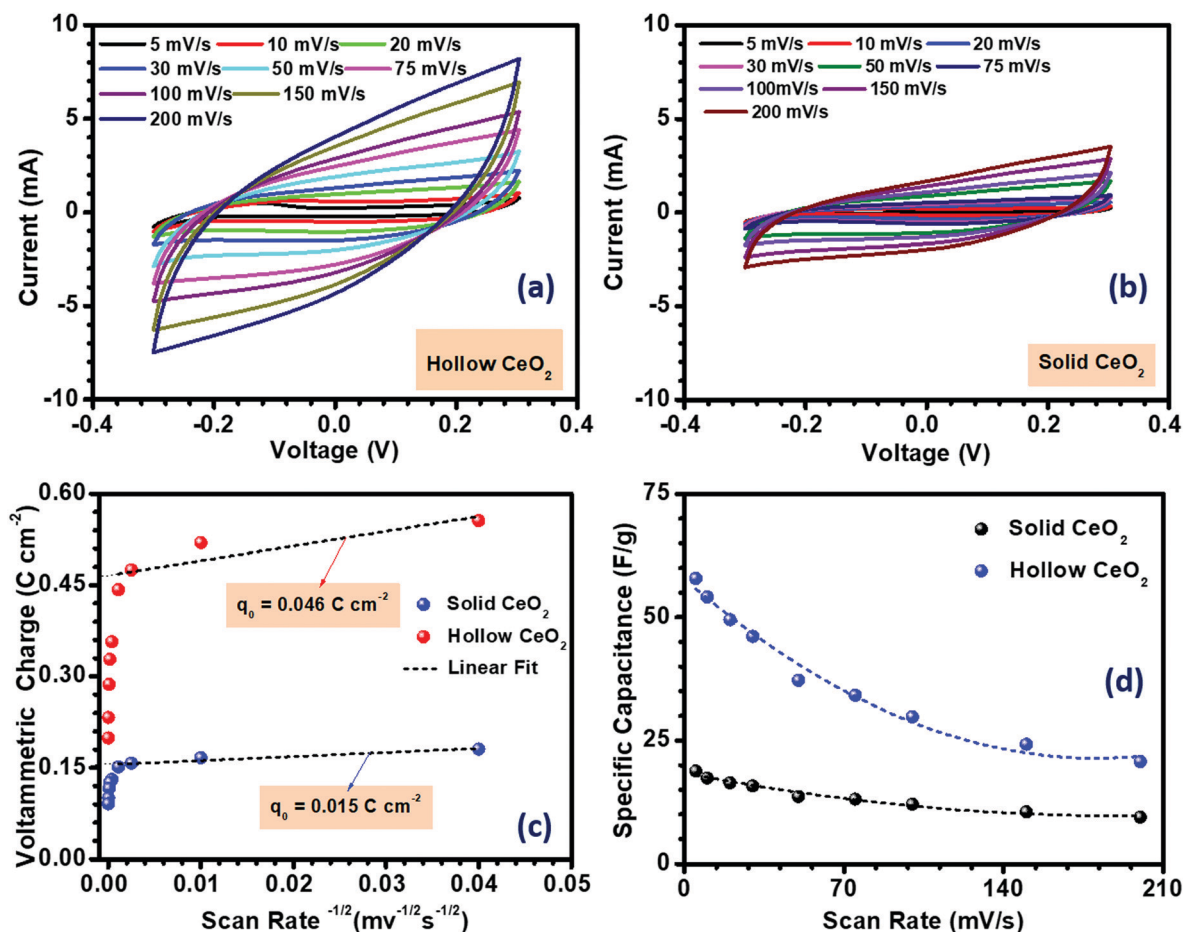
Fig. 3 (a and b) CV profiles, (c) charge accumulated and (d) specific capacitance variation with the scan rate in CeO_2 hollow nanospheres and CeO_2 solid nanoparticles.

were estimated as -3.81 and 1.97 mV, for hollow and solid CeO_2, respectively.
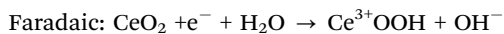
The higher performance can also be correlated with the accessible number of atoms/particles, which take part in the redox activities. Calculating the number of atoms on the surface will further prove the importance of these pseudo 2-D structures as they may have similar numbers of atoms taking part in the redox activity as they are in a similar sized 2-D structure. Considering a sphere of radius 6 nm, the number of atoms associated with the structures would be 33 401 and 8896 in solid and hollow structures, respectively. The calculation details are given in the ESI.† Among these atoms, the number of Ce atoms present could be estimated. The number of Ce atoms present would be 11 133 and 2965 in solid and hollow structures, respectively. But, effectively, the number of atoms taking part in redox activity would be 2931 and [A(2931) + B(2615)] = 5546, in solid and hollow spheres, respectively. This means that the hollow particle would not only be lighter but also ensure more number of atoms taking part in the redox activity. Additionally, one can ask: what is the effective ratio of the atoms participating in an electrochemical reaction in these particles? Normal electrodes are made of 1 mg cm^{-2} mass loading. From this, if we calculate the number of atoms, we can see that the 6 nm hollow

CeO_2 particle has 4 times higher Ce atoms in the electrode. This is shown in Scheme 2(b). The ratio will increase if the sphere size increases.

3.3 Electrochemical characterization of CeO_2

The electrochemical performance of hollow CeO_2 nanospheres, which could be considered as a pseudo-2-D structure, and solid CeO_2 nanoparticles is discussed below. Initially, the three electrode measurements were performed in 3 M KOH electrolyte, within a stable potential window of 0.6 V (from -0.3 to 0.3 V). The electrochemical performance of hollow and solid CeO_2 was also investigated in acidic electrolyte, *i.e.* 1 M H_2SO_4. The corresponding results are given in the ESI† (Fig. S26). The active mass of the materials was kept at $\sim$1 mg cm^{-2}, in both cases. Fig. 3(a) and (b) depict the CV profiles, as a function of scan rate. The redox peaks were visible in the CV curves, confirming the pseudocapacitive nature of CeO_2. The charge storage mechanism of CeO_2 based nanostructures in aqueous KOH depends on two mechanisms: (i) surface adsorption/desorption of K$^+$ ions and (ii) intercalation/de-intercalation of K$^+$ ions on the surface of the hollow CeO_2 structure. It can be represented as:[41]

Non-faradaic: $(CeO_2)_{Surface} + K^+ \leftrightarrow (CeO_2K^+)_{Surface}$

Faradaic: $CeO_2 + e^- + H_2O \rightarrow Ce^{3+}OOH + OH^-$

$Ce^{3+}OOH + e^- + OH^- \rightarrow CeO_2 + H_2O$

The K^+ ions have a smaller solvation radius and higher mobility in the electrolyte solution. Therefore, it gives better insertion/de-insertion capability. The shape of the CV curves for both the hollow and solid CeO_2 based electrodes, measured at different scan rates, indicated the pseudocapacitance nature. In the electrolyte solution, the hollow and solid CeO_2 electrodes received K^+ electrolyte ions on their surface leading to oxidation. The formula used to determine the specific capacitance from the CV profiles is given in Fig. S12 (ESI†). The estimated specific capacitance, using CV measurement, is given in Fig. 3(d). The maximum specific capacitances of the hollow and solid CeO_2 at 5 mV s^{-1} scan rate were 58 and 19 F g^{-1}, respectively. The specific capacitance values decreased with increasing scan rate, as shown in Fig. 3(d). The much higher specific capacitance in hollow CeO_2 contributed to all the inferences that were mentioned earlier. The high performance hollow CeO_2 would be useful as it would provide a higher number of redox active atoms to take part in the reaction, improved electrolyte diffusion, formation of an enhanced number of double layers, and higher surface charge.

From the Randles–Sevcik equation, the redox peak current was calculated and its linear relationship with the square root of the scan rate is shown in Fig. S10 (ESI†) for both the electrode materials. The linear relationship suggests that the electrode surface reactions, at all scan rates, were diffusion-controlled. The redox peaks involved K^+ ion diffusion from the electrolyte to the electrode surface during the reduction and oxidation processes. The active sites of the material perform a crucial role in the determination of the voltammetric charge. Again, the active site directly depends on the surface area of the coated material. The voltammetric charge ($q*$) was calculated using the following equation:[42]

$$q* = \frac{\int I \, dV}{As}$$

where, s, I, V and A denote the scan rate, voltammetric current (mA), potential (mV) and geometric area of the electrode (cm^2), respectively. Additionally, $q*$ can be expressed as:

$$q* = q_0 + s^{-1/2}$$

where, q_0 is the charge measured by the double layer and s is the scan rate. Fig. 3(c) depicts the $q*$ vs. $s^{-1/2}$ curve for hollow CeO_2. The curve indicated that the adsorbed charges on the surface of the electrode were decreasing with increasing scan rate. This type of curve has also been observed in other metal oxides, showing pseudocapacitive behaviour, such as RuO_2, IrO_2, etc.[43] The enhancement in the adsorption of charges on the electrode surface leads to a higher number of ions interacting with active sites of the electrode material. This result was a convoluted picture of the contribution from double-layer capacitance and pseudocapacitance. In this case, the adsorbed charge was ~ 46 mC cm^{-2} and ~ 15 mC cm^{-2} for hollow and

solid CeO_2, respectively, at 5 mV s^{-1} scan rate. This once again indicated that the hollow CeO_2 electrode has a high number of active sites, which increases the surface adsorption capacity, leading to enhanced electrochemical performance. The galvanostatic charge–discharge curves of hollow and solid CeO_2 electrodes at different current densities are shown in Fig. 4(a) and (b). The maximum specific capacitances of hollow and solid CeO_2 were estimated to be 166 and 63 F g^{-1}, respectively, at 1 A g^{-1} current density. The formula to calculate the specific capacitance from the CD profiles is given in the ESI.† The variation of specific capacitance value with increasing current density is shown in Fig. 4(c). The contribution of surface and diffusion capacitance for both CeO_2 using Dunn's method is shown in Fig. S13(a)–(e) (ESI†).

The conductivity of both nanostructures was measured using a two-probe approach. As shown in Fig. S14 (ESI†), the conductivity of the hollow CeO_2 was observed to be $\sim 3.31 \times 10^{-3}$ Ω^{-1} cm^{-1}, while the solid structure had a conductivity of $\sim 2.82 \times 10^{-3}$ Ω^{-1} cm^{-1}. The higher surface area and porosity of hollow CeO_2 could be related to its higher specific capacitance.[44] The high surface area and microporous structure of the hollow nanospheres would generate more active sites in the electrode material, allowing more K^+ ions to diffuse through the electrode–electrolyte interface.[45]

Another important parameter of any charge storage device for practical application is its cycling stability. Fig. 4(d) shows the cycling performance of both CeO_2 based nanostructures. The materials were subjected to repetitive charging and discharging at a constant current density of 2 A g^{-1} in the potential range of -0.3 to 0.3 V for 3000 cycles. Primarily, capacitance degradation was observed after 2000 cycles. After 3000 cycles, the specific capacitance value was $\sim 91\%$ for the hollow structure and $\sim 86\%$ for the solid material.

The Coulombic efficiency was calculated by using the equation:

$$\eta = \frac{t_d}{t_c} \times 100\%$$

where η is the Coulombic efficiency (%), and t_d and t_c are the discharging and charging time, respectively. The nearly triangular charge–discharge profiles were found to give a Coulombic efficiency of $\sim 88\%$ and $\sim 76\%$ for hollow and solid structures, respectively, at 5 A g^{-1} current density, as shown in Fig. S15 (ESI†). The Coulombic efficiency at other current densities is given in Table S7 (ESI†).

3.3. (a) Mechanism behind the enhancement of capacitance in pseudo 2-D-hollow nanostructures

The major reasons leading to higher performance in pseudo 2-D-nanostructures are mentioned below:

(a) The high surface area of hollow CeO_2 would lead to higher redox activity.

(b) The opening of the cavity makes the inner surface of the particle accessible to the incoming ions, which increases the net charge collection at the electrodes.

(c) Hollow CeO_2 spheres provide a lower diffusion coefficient, which reduces hindrance to the incoming solvated ions for accessing the interior surface of the core.
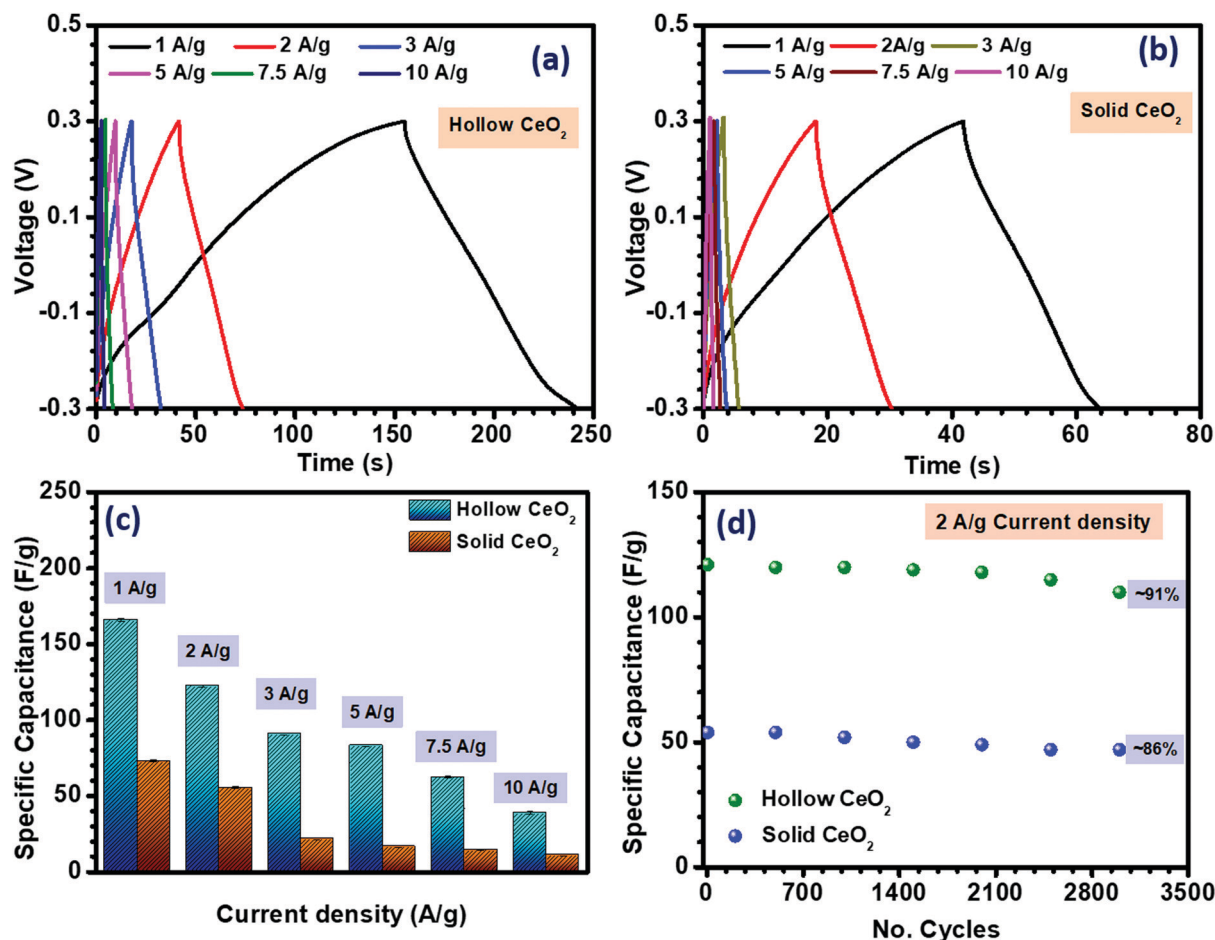
Fig. 4 (a and b) CD profiles, (c) specific capacitance from the CD profile and (d) cycling data of CeO_2 hollow and solid nanoparticles.

(d) The cavity of the hollow spheres also provides a high volume for ion adsorption, which ensures good cycling efficiency to these materials, as reported in some recent reports.
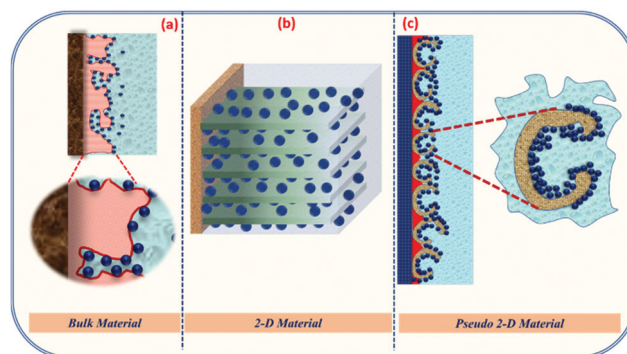
(f) Hollow structures will be able to compensate for volume charges as a function of internal heating during cycling.

These are schematically shown in Scheme 3. For solid structures, the surface facing the electrolyte will only accommodate the charges to collect near its surface. When these solid structures are converted to hollow structures, then the interior of the hollow structures, as well as some part of the exterior, will store charges.

3.4. Combining real 2-D structures with pseudo 2-D nanostructures

It is clear that hollow CeO_2 can deliver performance as a 2-D structure. As mentioned earlier, hybrid type supercapacitors are able to deliver high specific capacitance, energy and power density. Therefore, using a carbon-based counter electrode would be the way forward. Generally, activated carbon-based electrodes are used, as these particles have much higher specific capacitance. Over the last few decades, ever since the discovery of graphene or graphitic carbon-based layered structures, their use as a counter electrode has gained immense popularity. Even though these 2-D structures may have lower surface area than activated carbon, improved channels and

electrolyte intercalation leads to high redox activity, which ensures higher specific capacitance. Combining pseudo 2-D metal oxides with real 2-D carbon structures would be interesting. Therefore, we chose a fast emerging 2-D carbon based material, *i.e.* graphitic carbon nitride (gC_3N_4). A preliminary study showed that gC_3N_4 has much higher performance than activated carbon, as given in the ESI.† The electrochemical measurement showed that gC_3N_4 had a specific capacitance of 32 F g^{-1}, while activated carbon achieved 22 F g^{-1} at the same scan rate of 10 mV s^{-1} in

Scheme 3 Charge storage mechanism of the (a) bulk material, (b) 2-D material and (c) hollow material (porous 2-D).

Table 1 Comparison table of 2-D-gC$_3$N$_4$ and activated carbon

Material	Specific surface area (m^2 g^{-1})	Specific capacitance (F g^{-1})	
		Scan rate (10 mV s^{-1})	Current density (1 A g^{-1})
Activated Carbon	71	22	35
2-D-gC$_3$N$_4$	20.15	32	46

3 M KOH, as shown in Table 1. The pseudocapacitance behaviour of 2-D-gC$_3$N$_4$ could be attributed to the tris-triazine unit connected with planar amino groups in each layer. The weak van der Waals force of the amino group acts between the layers, which enhances the specific capacitance.[46]

The formation of a 2-D-layered structure of graphitic carbon nitride is discernible from the formation of the tris-triazine structure, confirmed by the XRD data shown in Fig. S16(a) (ESI†). The formation of particles with a layered structure could be easily inferred by examining the AFM, SEM and TEM pictures, respectively, shown in Fig. S16(b)–(d) (ESI†). The FTIR result is shown in Fig. S17 (ESI†). The C and N element present in the 2-D graphite carbon nitrate structure was confirmed by EDX analysis, as shown in Fig. S18 (ESI†).

The electrochemical performance of 2-D-gC$_3$N$_4$ was investigated in the potential range from 0.0 to −1.0 V (vs. Ag/AgCl) at different scan rates and current densities, in 3 M KOH. The corresponding findings are shown in Fig. S19(a) and (b) (ESI†), respectively. The specific capacitance was calculated from the CV and CD curves, and their variation with the scan rate and current density is shown in Fig. S19(c) and (d) (ESI†). The detailed discussion regarding the electrochemical performance of 2-D-gC$_3$N$_4$ is given in the ESI.†

Asymmetric supercapacitors were fabricated with CeO$_2$ nanostructure as the positive electrode and 2-D graphite carbon nitride as the negative electrode. Before fabricating the device, the required weight ratio of the materials was calculated, which would ensure the essential charge balanced condition. The desired mass ratio was calculated using the following mass-balance relations:

$$q_+ = C_+ \times V_+ \times m_+$$

$$q_- = C_- \times V_- \times m_-$$

$$\frac{m_+}{m_-} = \frac{C_-}{C_+} \times \frac{V_-}{V_+}$$

where, q_+ and q_- are the charge stored, m_+ and m_- are the mass, and C_+ and C_- are the capacitance value of the positive and negative electrodes at the same scan rate. V_+ and V_- denote the potential window of the positive and negative electrode material, respectively. For the present case, the required mass ratio
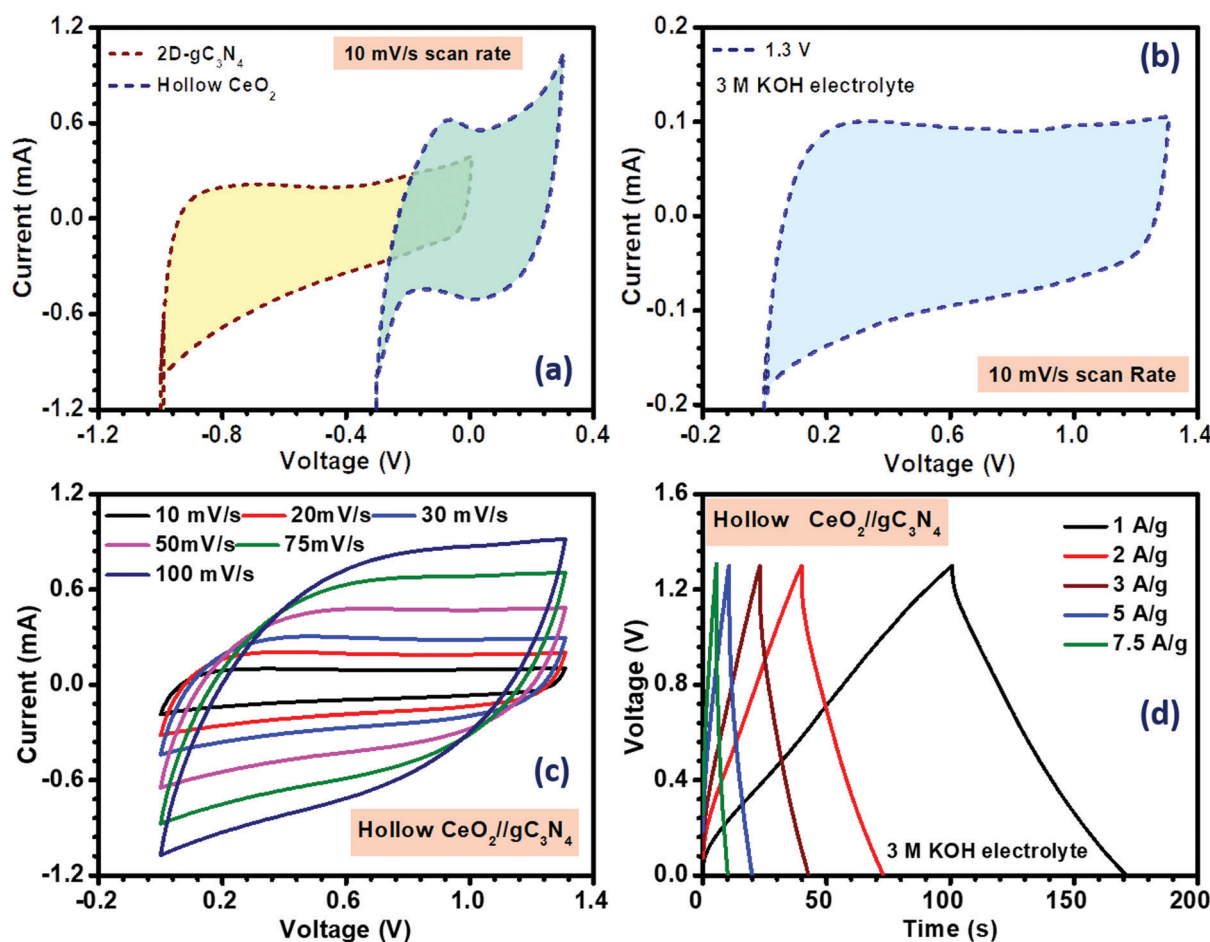

Fig. 5 (a) Window comparison at fixed scan rate, (b) window optimization, (c) CV and (d) CD profiles of the hollow CeO$_2$‖gC$_3$N$_4$ asymmetric device.
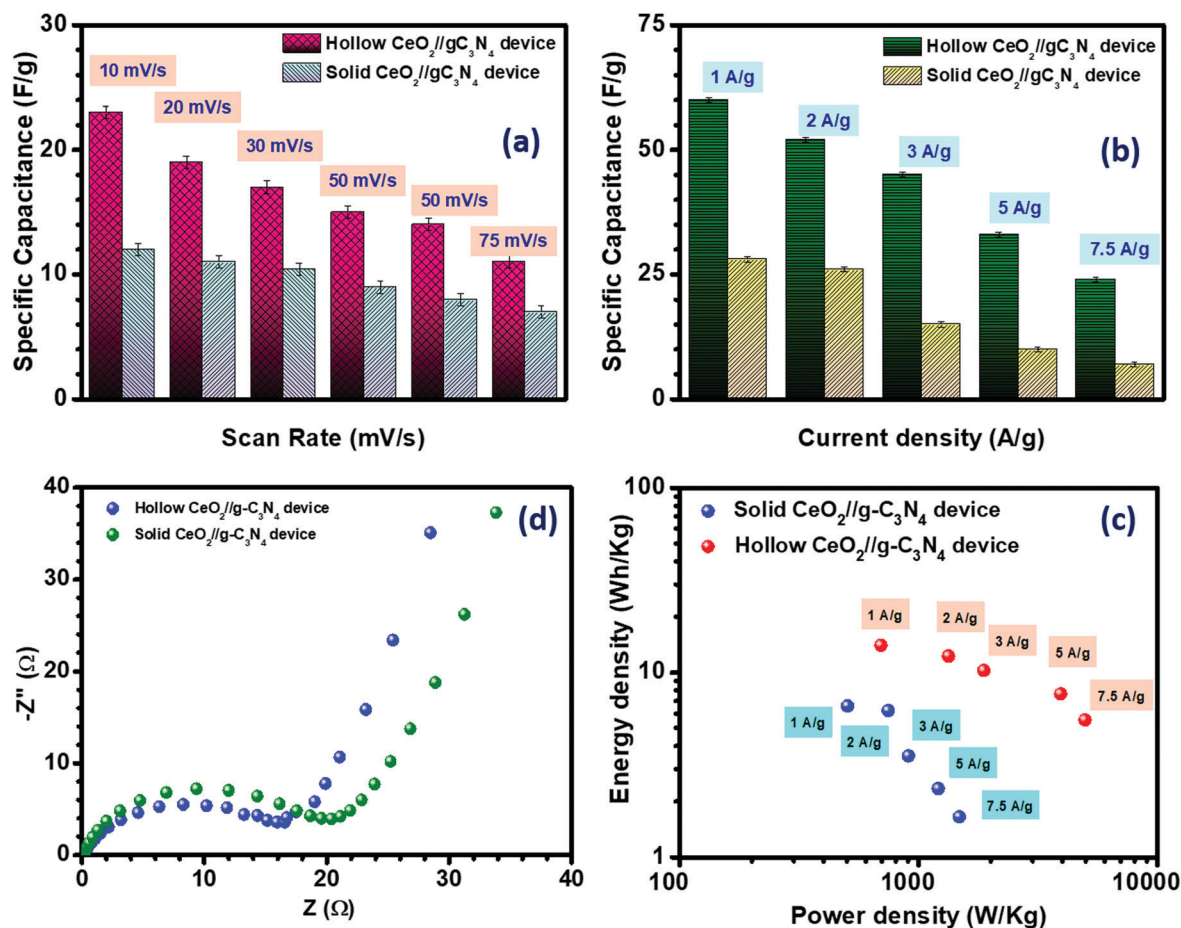

Fig. 6 Specific capacitance from (a) CV and (b) CD, (c) Nyquist plot and (d) Ragone plot of hollow CeO$_2$‖gC$_3$N$_4$ and solid CeO$_2$‖gC$_3$N$_4$ devices.

of the positive and negative electrode was obtained as ∼1.2. The fabricated asymmetric device was found to achieve a stable potential window of 1.3 V, as shown in Fig. 5(a) and (b). The electrochemical results of the asymmetric device of solid CeO$_2$‖gC$_3$N$_4$ are depicted in Fig. S24(a) and (b) (ESI†). The electrochemical performance of the hollow CeO$_2$‖gC$_3$N$_4$ device was analysed using CV curves within the above-mentioned potential window, at scan rates ranging from 10 to 100 mV s^{-1}. The device showed nearly rectangular CV profiles, with the expected redox peaks, as shown in Fig. 5(c). This indicated a synergistic combination of pseudocapacitance and EDLC behaviour. The shape of the CV curves did not change with increasing cell voltage or by increasing scan rates. It was clear that there was no O$_2$ or H$_2$ evolution within this optimized potential window. The device was also characterized using CD measurements. The obtained specific capacitance using CV data analysis is given in Table S6 (ESI†). The specific capacitance calculated for the asymmetric device using a hollow and solid CeO$_2$‖gC$_3$N$_4$ combination, from CV analysis, is listed in Table S6 (ESI†). Fig. 5(d) depicts the charge–discharge profiles of the device at different current densities. The variation of specific capacitance with both scan rate and current density is shown in Fig. 6(a) and (b), respectively. The specific capacitances from CD for the asymmetric devices using solid and hollow structures are given in Table 2.

The asymmetric devices fabricated using 1 M H$_2$SO$_4$ were also electrochemically investigated and they showed a stable potential window of 1.5 V, as shown in Fig. S27 (ESI†). The corresponding CD profiles and Ragone plots are given in Fig. S28 (ESI†).

The equivalent series resistance (ESR) was calculated using the following formula:[47,48]

$$\mathrm{ESR} = \frac{V}{2I}$$

where V is the voltage drop at the start of the discharge cycle and I is the corresponding current in ampere. The calculated equivalent series resistance was found to be ∼0.4 Ω cm^{-2}, at 1 A g^{-1} current density, for hollow CeO$_2$‖gC$_3$N$_4$, as shown in

Table 2 Specific capacitance of the hollow and solid CeO$_2$‖gC$_3$N$_4$ device from CD

Current density (A g^{-1})	Specific capacitance (F g^{-1})	
	Hollow CeO$_2$‖gC$_3$N$_4$	Solid CeO$_2$‖gC$_3$N$_4$
1	60	28
2	52	26
3	45	15
5	33	10
7.5	24	07

Table 3 Comparison of supercapacitor performance of different CeO_2-based nanostructures

Material (current collector)	Specific capacitance (F g^{-1})	Electrolyte	Device	Energy density (W h kg^{-1})	Power density (kW kg^{-1})	Ref.
CeO_2 nanorod (Ni Foam)	154	2 M KOH	$CeO_2\|AC$	5.83	0.75	49
CeO_2 nanoparticle/graphene composite (Ni Foam)	208	3 M KOH	—	—	18	29
Nano CeO_2/AC composite (carbon paper)	162	1 M HCl	$CeO_2/AC\|AC$	4.86	3.5	50
CeO_2 nanoparticle (Ni foam)	78.5	6 M KOH	—	—	—	51
Hollow CeO_2-MWCNT (Ni foam)	450	6 M KOH	Hollow CeO_2-MWCNT$\|AC$	26.2	10.6	
Porous CeO_2 (Ni foam)	135	1 M KOH	—	—	—	52
CeO_2 nanoparticle (Ni foam)	98	3 M KOH	—	—	—	53
CeO_2 nanorod (Ni foam)	162					
CeO_2 nanocube (Ni foam)	149					
Hollow CeO_2 (graphite sheet)	166	3 M KOH	Hollow $CeO_2|$2-D-gC_3N_4	14.33	0.70	Present work

Fig. S24(d) (ESI†). The Nyquist plot of the hollow and solid $CeO_2\|gC_3N_4$ device is shown in Fig. 6(c). The Nyquist plot consisted of two distinct regions, separated with a semi-circular region (high frequency) and straight-line along with an imaginary axis region (low frequency). The semicircle represents the charge transfer resistance (R_{ct}), which was estimated as ~ 2.3 and $8.5\ \Omega$ for the hollow and solid $CeO_2\|gC_3N_4$ devices, respectively. The lower charge transfer resistance could be attributed to the enhanced diffusive resistance of negative ions at the porous electrode. The straight line (low-frequency region) was more towards the imaginary axis, indicating good capacitive behaviour in the hollow $CeO_2\|gC_3N_4$ device. The corresponding Bode plots of both the devices are shown in Fig. S29 (ESI†).

As mentioned earlier, cycling stability is one of the important parameters for practical application of supercapacitors. The cycling stability of both the fabricated devices was measured up to 3000 cycles at 2 A g^{-1} current density and the results are given in Fig. S20(c) (ESI†). The capacitance retention after 3000 cycles was $\sim 96.15\%$ for the hollow $CeO_2\|gC_3N_4$ device and $\sim 88.4\%$ for the solid $CeO_2\|gC_3N_4$ device, indicating excellent cycling stability. The corresponding physicochemical characterization of the electrode after the cycling stability test is shown in Fig. S25 (ESI†).

It is now well-known that supercapacitor devices are popular because of their good balance between energy and power density. The energy density and the power density of the solid and hollow $CeO_2\|gC_3N_4$ devices were calculated using the following equations:

$$E = \frac{1}{2}CV^2$$

$$P = \frac{E}{t}$$

where E is the energy density (W h kg^{-1}); C is the specific capacitance (F g^{-1}); V is the voltage window (V) and P is the power density (W kg^{-1}). The fabricated hollow $CeO_2\|gC_3N_4$ device exhibited an excellent energy density of ~ 14.33 W h kg^{-1} along with a power density of ~ 700 W kg^{-1}, whereas the solid $CeO_2\|gC_3N_4$ device showed an energy density of ~ 6.67 W h kg^{-1} along with a power density of ~ 505 W kg^{-1} at 1 A g^{-1} current density, as shown in Fig. 6(d). The high energy density obtained at the higher current density is reported for the first time for a hollow

CeO_2 based supercapacitor, as shown in Table 3. The excellent performance of this device could therefore be directly linked to the use of the hollow nanostructure.

4. Conclusions

It is clearly shown that hollow particles can actually be considered as pseudo 2-D type structures. It is not only their higher specific area that leads to higher electrochemical performance. In reality, the improvement is driven by additional factors that involve stabilization of layered type characteristics but with stable channels for ion diffusion. This improves ion interaction with the solid and induces improvement in both EDLC and pseudocapacitance. Contrary to most results, it is shown that rare earth element-based oxides can also become useful for energy storage devices, provided their particles with hollow morphologies are used. Consistent explanations are based on corroborating theory and experimentally obtained results. The importance of combining pseudo 2-D nanostructures of metal oxides with real 2-D carbon-based materials to develop hybrid supercapacitors is unequivocally established. The fabricated asymmetric supercapacitors using hollow CeO_2 and gC_3N_4 as positive and negative electrodes, would deliver maximum specific capacitance of ~ 60 F g^{-1} at 1 A g^{-1} current density, with an excellent energy density of ~ 14.20 W h kg^{-1} and power density of 700 W kg^{-1}.

Conflicts of interest

There are no conflicts to declare.

Acknowledgements

References

1 G. H. An, J. Hong, S. Pak, Y. Cho, S. Lee, B. Hou and S. Cha, Zn–ion supercapacitors: 2D metal Zn nanostructure electrodes for high-performance zn ion supercapacitors (Adv. Energy Mater. 3/2020), *Adv. Energy Mater.*, 2020, **10**, 2070010.

2 X. Zhang, L. Hou, A. Ciesielski and P. Samorì, 2D materials beyond graphene for high-performance energy storage applications, *Adv. Energy Mater.*, 2016, **6**, 1600671.

3 L. Lin, J. Chen, D. Liu, X. Li, G. G. Wallace and S. Zhang, Engineering 2D materials: A viable pathway for improved electrochemical energy storage, *Adv. Energy Mater.*, 2020, **10**, 2002621.

4 A. VahidMohammadi, J. Rosen and Y. Gogotsi, The world of two-dimensional carbides and nitrides (MXenes), *Science*, 2021, **372**, abf1581.

5 H. W. Guo, Z. Hu, Z. B. Liu and J. G. Tian, Stacking of 2D materials, *Adv. Funct. Mater.*, 2020, **31**, 2007810.

6 Y. Wei, X. Tang, J. Shang, L. Ju and L. Kou, Two-dimensional functional materials: From properties to potential applications, *Int. J. Smart Nano Mater.*, 2020, **11**, 247–264.

7 X. Tang, X. Guo, W. Wu and G. Wang, 2D metal carbides and nitrides (MXenes) as high-performance electrode materials for lithium-based batteries, *Adv. Energy Mater.*, 2018, **8**, 1801897.

8 B. Wang, Y. Sun, H. Ding, X. Zhao, L. Zhang, J. Bai and K. Liu, Bioelectronics-related 2D materials beyond graphene: Fundamentals, properties, and applications, *Adv. Funct. Mater.*, 2020, **30**, 2003732.

9 N. R. Glavin, R. Rao, V. Varshney, E. Bianco, A. Apte, A. Roy, E. Ringe and P. M. Ajayan, Emerging applications of elemental 2D materials, *Adv. Mater.*, 2020, **32**, e1904302.

10 P.-K. Yang and C.-P. Lee, Applied Electromechanical Devices and Machines for Electric Mobility Solutions, *2D-layered nanomaterials for energy harvesting and sensing applications*, 2020.

11 C. Guan, X. Liu, W. Ren, X. Li, C. Cheng and J. Wang, Rational design of metal–organic framework derived hollow $NiCo_2O_4$ arrays for flexible supercapacitor and electrocatalysis, *Adv. Energy Mater.*, 2017, **7**, 1602391.

12 V. Sharma, S. Biswas and A. Chandra, Need for revisiting the use of magnetic oxides as electrode materials in supercapacitors: Unequivocal evidence of significant variation in specific capacitance under variable magnetic field, *Adv. Energy Mater.*, 2018, **8**, 1800573.

13 A. Kozhakhmetov, R. Torsi, C. Y. Chen and J. A. Robinson, Scalable low-temperature synthesis of two-dimensional materials beyond graphene, *JPhys Mater.*, 2020, **4**, 012001.

14 G. Korotcenkov, Current trends in nanomaterials for metal oxide-based conductometric gas sensors: Advantages and limitations. Part 1: 1D and 2D nanostructures, *Nanomaterials*, 2020, **10**, 1392.

15 B. K. Kim, S. Sy, A. Yu and J. Zhang, Electrochemical supercapacitors for energy storage and conversion, in *Handbook of clean energy systems*, 2015, pp. 1–25.

16 M. Guan, Q. Wang, X. Zhang, J. Bao, X. Gong and Y. Liu, Two-dimensional transition metal oxide and hydroxide-based hierarchical architectures for advanced supercapacitor materials, *Front. Chem.*, 2020, **8**, 390.

17 P. Kumbhakar, C. Chowde Gowda, P. L. Mahapatra, M. Mukherjee, K. D. Malviya, M. Chaker, A. Chandra, B. Lahiri, P. M. Ajayan, D. Jariwala, A. Singh and C. S. Tiwary, Emerging 2D metal oxides and their applications, *Mater. Today*, 2021, **45**, 142–168.

18 S. M. Mali, D. J. Late and B. R. Sathe, Supercapacitors based on two-dimensional metal oxides, hydroxides, and its graphene-based hybrids, *Fundam. Supercapacitor Appl. 2D Mater.*, 2021, 193–215.

19 S. Zheng, Y. Sun, H. Xue, P. Braunstein, W. Huang and H. Pang, Dual-ligand and hard-soft-acid-base strategies to optimize metal–organic framework nanocrystals for stable electrochemical cycling performance, *Natl. Sci. Rev.*, 2021, nwab197.

20 Y. Bai, C. Liu, T. Chen, W. Li, S. Zheng, Y. Pi, Y. Luo and H. Pang, MXene-copper/cobalt hybrids via Lewis acidic molten salts etching for high performance symmetric supercapacitors, *Angew. Chem., Int. Ed.*, 2021, **60**, 25318–25322.

21 C. Liu, Y. Bai, W. Li, F. Yang, G. Zhang and H. Pang, *In situ* growth of three-dimensional MXene/metal–organic framework composites for high-performance supercapacitors, *Angew. Chem., Int. Ed.*, 2022, **61**, e202116282.

22 B. Li, P. Gu, Y. Feng, G. Zhang, K. Huang, H. Xue and H. Pang, Ultrathin nickel–cobalt phosphate 2D nanosheets for electrochemical energy storage under aqueous/solid-state electrolyte, *Adv. Funct. Mater.*, 2017, **27**, 1605784.

23 X. Li, J. Wei, Q. Li, S. Zheng, Y. Xu, P. Du, C. Chen, J. Zhao, H. Xue, Q. Xu and H. Pang, Nitrogen-doped cobalt oxide nanostructures derived from cobalt–alanine complexes for high-performance oxygen evolution reactions, *Adv. Funct. Mater.*, 2018, **28**, 1800886.

24 S. Wu, Y. Chen, T. Jiao, J. Zhou, J. Cheng, B. Liu, S. Yang, K. Zhang and W. Zhang, An aqueous zn–ion hybrid supercapacitor with high energy density and ultrastability up to 80 000 Cycles, *Adv. Energy Mater.*, 2019, **9**, 1902915.

25 J. Ruan, F. Mo, Z. Chen, M. Liu, S. Zheng, R. Wu, F. Fang, Y. Song and D. Sun, Rational construction of nitrogen-doped hierarchical dual-carbon for advanced potassium-ion hybrid capacitors, *Adv. Energy Mater.*, 2020, **10**, 1904045.

26 H. Tang, J. Yao and Y. Zhu, Recent developments and future prospects for zinc–ion hybrid capacitors: A review, *Adv. Energy Mater.*, 2021, **11**, 2003994.

27 N. Maheswari and G. Muralidharan, Hexagonal CeO_2 nanostructures: An efficient electrode material for supercapacitors, *Dalton Trans.*, 2016, **45**, 14352–14362.

28 N. Padmanathan and S. Selladurai, Shape controlled synthesis of CeO_2 nanostructures for high performance supercapacitor electrodes, *RSC Adv.*, 2014, **4**, 6527.

29 Y. Wang, C. X. Guo, J. Liu, T. Chen, H. Yang and C. M. Li, CeO_2 nanoparticles/graphene nanocomposite-based high performance supercapacitor, *Dalton Trans.*, 2011, **40**, 6388–6391.

30 T. Saravanan, M. Shanmugam, P. Anandan, M. Azhagurajan, K. Pazhanivel, M. Arivanandhan, Y. Hayakawa and R. Jayavel, Facile synthesis of graphene–CeO_2 nanocomposites with enhanced electrochemical properties for supercapacitors, *Dalton Trans.*, 2015, **44**, 9901–9908.

31 J. Hocker, J. O. Krisponeit, T. Schmidt, J. Falta and J. I. Flege, The cubic-to-hexagonal phase transition of cerium oxide particles: Dynamics and structure, *Nanoscale*, 2017, **9**, 9352–9358.

32 N. Kainbayev, M. Sriubas, D. Virbukas, Z. Rutkuniene, K. Bockute, S. Bolegenova and G. Laukaitis, Raman study of nanocrystalline-doped ceria oxide thin films, *Coatings*, 2020, **10**, 432.

33 W. H. Weber, K. C. Hass and J. R. McBride, Raman study of CeO_2: Second-order scattering, lattice dynamics, and particle-size effects, *Phys. Rev. B: Condens. Matter Mater. Phys.*, 1993, **48**, 178–185.

34 A. M. Burow, T. Wende, M. Sierka, R. Wlodarczyk, J. Sauer, P. Claes, L. Jiang, G. Meijer, P. Lievens and K. R. Asmis, Structures and vibrational spectroscopy of partially reduced gas-phase cerium oxide clusters, *Phys. Chem. Chem. Phys.*, 2011, **13**, 19393–19400.

35 S. Biswas, V. Sharma, D. Mandal, A. Chowdhury, M. Chakravarty, S. Priya, C. C. Gowda, P. De, I. Singh and A. Chandra, Hollow nanostructures of metal oxides as emerging electrode materials for high performance supercapacitors, *CrystEngComm*, 2020, **22**, 1633–1644.

36 D. Mandal, S. Biswas, A. Chowdhury, D. De, C. S. Tiwary, A. N. Gupta, T. Singh and A. Chandra, Hierarchical cage-frame type nanostructure of CeO_2 for bio sensing applications: From glucose to protein detection, *Nanotechnology*, 2020, **32**, 025504.

37 K. Cendrowski, W. Kukulka, T. Kedzierski, S. Zhang and E. Mijowska, Poly(vinylidene fluoride) and carbon derivative structures from eco-friendly MOF-5 for supercapacitor electrode preparation with improved electrochemical performance, *Nanomaterials*, 2018, **8**, 890.

38 T. Nguyen and M. F. Montemor, Metal oxide and hydroxide-based aqueous supercapacitors: From charge storage mechanisms and functional electrode engineering to need-tailored devices, *Adv. Sci.*, 2019, **6**, 1801797.

39 G. Duan, F. Lv, W. Cai, Y. Luo, Y. Li and G. Liu, General synthesis of 2D ordered hollow sphere arrays based on nonshadow deposition dominated colloidal lithography, *Langmuir*, 2010, **26**, 6295–6302.

40 S. Biswas, V. Sharma, T. Singh and A. Chandra, External vibrations can destroy the specific capacitance of supercapacitors – from experimental proof to theoretical explanations, *J. Mater. Chem. A*, 2021, **9**, 6460–6468.

41 Y. Luo, T. Yang, Q. Zhao and M. Zhang, CeO_2/CNTs hybrid with high performance as electrode materials for supercapacitor, *J. Alloys Compd.*, 2017, **729**, 64–70.

42 A. Chowdhury, S. Biswas, T. Singh and A. Chandra, Redox mediator induced electrochemical reactions at the electrode–electrolyte interface: Making sodium-ion supercapacitors a competitive technology, *Electrochemical Science Advances*, 2021.

43 W. Sun, Y. Song, X. Q. Gong, L. M. Cao and J. Yang, Hollandite structure K(x approximately 0.25)IrO_2 catalyst with highly efficient oxygen evolution reaction, *ACS Appl. Mater. Interfaces*, 2016, **8**, 820–826.

44 M. Vanitha, Keerthi, P. Cao and N. Balasubramanian, Ag nanocrystals anchored CeO_2/graphene nanocomposite for enhanced supercapacitor applications, *J. Alloys Compd.*, 2015, **644**, 534–544.

45 N. Padmanathan and S. Selladurai, Electrochemical capacitance of porous NiO–CeO_2 binary oxide synthesized via sol–gel technique for supercapacitor, *Ionics*, 2013, **20**, 409–420.

46 G. Algara-Siller, N. Severin, S. Y. Chong, T. Bjorkman, R. G. Palgrave, A. Laybourn, M. Antonietti, Y. Z. Khimyak, A. V. Krasheninnikov, J. P. Rabe, U. Kaiser, A. I. Cooper, A. Thomas and M. J. Bojdys, Triazine-based graphitic carbon nitride: A two-dimensional semiconductor, *Angew. Chem., Int. Ed.*, 2014, **53**, 7450–7455.

47 A. Chowdhury, R. Shukla, V. Sharma, S. Neogy, A. Chandra, V. Grover and A. K. Tyagi, Controlling reaction kinetics of layered zinc vanadate having brucite-like Zn–O layers supported by pyrovanadate pillars for use in supercapacitors, *J. Alloys Compd.*, 2020, **829**, 154479.

48 D. Mandal, P. L. Mahapatra, R. Kumari, P. Kumbhakar, A. Biswas, B. Lahiri, A. Chandra and C. S. Tiwary, Convert waste petroleum coke to multi-heteroatom self-doped graphene and its application as supercapacitors, *Emergent Mater.*, 2021, **4**, 531–544.

49 H. Wang, M. Liang, X. Zhang, D. Duan, W. Shi, Y. Song and Z. Sun, Novel CeO_2 nanorod framework prepared by dealloying for supercapacitors applications, *Ionics*, 2018, **24**, 2063–2072.

50 L. S. Aravinda, K. Udaya Bhat and B. Ramachandra Bhat, Nano CeO_2/activated carbon based composite electrodes for high performance supercapacitor, *Mater. Lett.*, 2013, **112**, 158–161.

51 Z.-J. Sun, H. Ge, S. Zhu, X.-M. Cao, X. Guo, Z.-H. Xiu, Z.-H. Huang, H. Li, T. Ma and X.-M. Song, Versatile template-free construction of hollow nanostructured CeO_2 induced by functionalized carbon materials, *J. Mater. Chem. A*, 2019, **7**, 12008–12017.

52 K. Prasanna, P. Santhoshkumar, Y. N. Jo, I. N. Sivagami, S. H. Kang, Y. C. Joe and C. W. Lee, Highly porous CeO_2 nanostructures prepared via combustion synthesis for supercapacitor applications, *Appl. Surf. Sci.*, 2018, **449**, 454–460.

53 A. Jeyaranjan, T. S. Sakthivel, M. Molinari, D. C. Sayle and S. Seal, Morphology and crystal planes effects on supercapacitance of CeO_2 nanostructures: Electrochemical and molecular dynamics Studies, *Part. Part. Syst. Charact.*, 2018, **35**, 1800176.